



Analytical modelling and experimental study of the cladding characteristics of a laser powder-fed additive manufacturing process

Lijuan Zhao¹ · Haitao Yue¹ · Chenguang Guo¹ · Qiang Li¹ · Guangbo Hao²

Received: 18 March 2020 / Accepted: 21 July 2020 / Published online: 9 August 2020
© Springer-Verlag London Ltd., part of Springer Nature 2020

Abstract

To avoid the effects of the overlap phenomenon among powder particles, the concept of an effective particle number was introduced, and multi-parameter analytical models for laser powder-fed additive manufacturing (LPF-AM) cladding geometric characteristics were established based on the laws of energy and mass conservation. Experimental research on the LPF-AM of a FeCr alloy was carried out, and the theoretical results are discussed and compared with the experimental data from the perspective of the laser energy density and powder density. The results showed that the cladding area was proportional to both the laser energy density and powder density. The mixing area and dilution rate decreased gradually with increasing powder density, while they increased first and then decreased with increasing laser energy density. The analytical model calculation values fit well with the experimental measurements. The microstructure of the cladding layer and substrate showed good metallurgical bonding, and the micro-hardness variation from the mixing to the cladding zone ranged from 423 to 627 HV.

Keywords Laser powder-fed additive manufacturing · Laser energy attenuation · Analytical modelling · Cladding characteristics · Laser energy and powder density

1 Introduction

Laser powder-fed additive manufacturing (LPF-AM) can produce a high-performance cladding layer, that provides high-temperature resistance [1], corrosion resistance [2], wear resistance [3, 4] and fatigue resistance [5, 6], that significantly improves the surface performance and extends the service life of components at a decreased cost. During the LPF-AM process, the interaction of the laser beam and powder stream cause laser energy attenuation and affect the amount and distribution of the laser energy reaching the substrate [7, 8], which is one of the main factors affecting the forming accuracy and mechanical properties of cladding layers. Therefore, it is particularly important to study the effect of the powder stream on the laser energy attenuation and transfer, establish

a comprehensive theoretical description of the relationships between multi-parameters and forming characteristics based on the energy and mass conservation law and ultimately obtain a cladding layer with improved forming quality.

Scholars have researched the geometric characteristic model of the cladding layer and the trends of the process parameters. Lalas et al. [9] built clad characteristics models considering the process speed and feed rate, and the models were capable of predicting the cladding width and depth with reasonable accuracy at low and medium process speeds. Fathi et al. [10] presented a mathematical model to predict the temperature field, melt pool depth and dilution. The model validated by experiments was developed using the moving heat source method. Campanelli et al. [11] presented a mathematical model using the calculus of the optimal overlapping degree between adjacent layers and between successive tracks. Wang et al. [12] established a cladding geometry theoretical model that considers the process parameters and provides good predictions. Barekat et al. [13–15] and Mohammad et al. [16] systematically studied the empirical statistical relationship between the combination of process parameters and the cladding layer geometric characteristics with different powder materials by using linear regression analysis, and verified that the fitting and the measured values were well matched by correlation coefficients and

✉ Chenguang Guo
gchg_neu@163.com

¹ School of Mechanical Engineering, Liaoning Technical University, Fuxin, China

² Department of Electrical and Electronic Engineering, University College Cork, Cork, Ireland

parameter analysis. Ocelik et al. [17] presented a recursive model for the effective prediction of a coating layer profile formed by the overlap of a single track. Nenadl et al. [18] presented a versatile model for the prediction of the geometry of laser clad depositions formed by the overlap of individual tracks and layers as a 2D cross-sectional model. Huang et al. [19] produced a comprehensive analytical model for the LPF-AM process, and the deposition of Inconel 625 showed that the model could accurately predict the cladding geometry and catchment efficiency over the range of specific energy that corresponded to high forming quality. In the study by Shi et al. [20], the energy and mass conservation law and the regression algorithm were used together to establish the mathematical models that were used to study the relationship between the cladding layer geometry characteristics, and minor errors existed. Reddy et al. [21] developed models of the influence of process parameters (laser power, laser traverse speed and powder feed rate) on the powder deposition efficiency, dilution and porosity, and these models were used to successfully produce an optimized coating. Liu et al. [22] adopted a circular arc to describe the geometry profile of the cross section of single-track cladding that was confirmed by experiments. Xi et al. [23] replaced the geometry of the fusion zone by a polynomial function of the fourth degree, and the relationship among the thermal tension angle, the cladding width, the melting pool depth and the area of the fusion zone was established. The estimated results coincided with the measurement results very well. Zhu et al. [24] formulated an integrated model of the laser cladding repair process, and the model evaluated the width, contact angle or height of the cladding layer and dilution rate for given process parameters.

The above models were mostly established based on the cladding layer geometry, the energy conservation law and a multiple regression algorithm. However, the studies [25–27] found that due to the extinction effect of the powder stream, the energy reaching the molten pool and substrate through the powder stream would be attenuated by the nozzle structure, quantity of powder particles, powder characteristics and powder size; inevitably, the maximum attenuation rate reached 30% [26]. If the laser energy was attenuated too much by the powder stream, the molten pool may be undesirable. Blindly increasing the laser power or decreasing the quantity of powder particles reduces the surface quality and processing efficiency. Therefore, ignoring the impact of laser energy attenuation on the forming quality is undesirable, but relevant research has rarely been reported.

In this paper, the laser energy attenuation rate for the LPF-AM process was modelled via the powder stream characteristics and the effective number of powder particles that go through the coaxial powder feeding nozzle. Considering the laser attenuation rate and the energy and mass conservation law, multi-parameter analytical models of the cladding layer geometry (cladding area, mixing area and dilution) were

established. The LPF-AM experimental research of FeCr alloy single-track cladding was carried out, and the influence rules of laser energy density and powder density on the forming quality were analysed. The model validity was verified by comparing the model predicted values with the experimental data, and the microstructure and mechanical properties of the forming area were evaluated.

2 Analytical modelling

Due to the very short duration of the laser beam, powder stream and substrate and the complexity of the interactions, analytical models were developed in this study with the following assumptions.

- (1) The powder particles are spherical with the same radius r_p , and only the light-facing surface absorbs the laser beam energy [12].
- (2) The gas-powder stream has a steady-state flow and the powder stream speed is uniform and constant as the gas velocity near the nozzle outlet. The effects of the shielding gas, gravity and drag force are considered negligible [8, 19].
- (3) The thermo-physical properties of the powder, molten pool and substrate are considered to be temperature independent [12, 19, 20].
- (4) The effective energy absorbed by the melting pool is used for powder melting and the temperature rise of the molten pool, and the alloy element diffusion behaviour between the liquid molten pool and substrate is ignored.
- (5) The heat-affected zone (HAZ) is adiabatic [20].

2.1 Laser energy attenuation rate

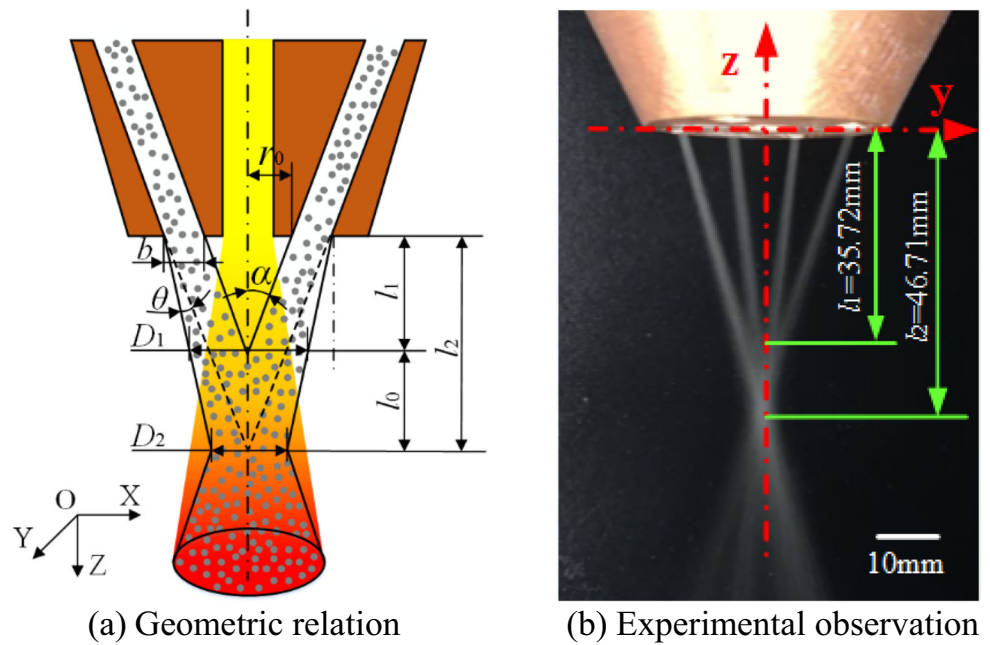
The geometry of the four-tube coaxial nozzle powder stream is shown in Fig. 1, where r_0 is the distance between the powder tube boundary and the central axis; b is the inner diameter of the powder tube; θ is the divergence angle; α is the included angle between the tube and the central axis; D_1 and D_2 are the upper and lower diameters of the powder stream respectively; l_1 and l_2 are the distance between the upper and lower focus of the powder stream and the powder outlet, respectively and l_0 is the focal length of the powder stream.

The following relational formula can be obtained by calculating the powder stream geometry according to the parameters shown in Fig. 1:

$$l_1 = \frac{r_0}{\tan \alpha} \quad (1)$$

$$l_2 = \frac{r_0 + b}{\tan \alpha} \quad (2)$$

Fig. 1 The geometry of the coaxial nozzle for the powder stream



$$l_0 = l_2 - l_1 = \frac{b}{\tan \alpha} \tag{3}$$

$$D_1 = 2 \left[(r_0 + b) - l_1 \tan(\alpha - \theta) \right] = 2 \left[(r_0 + b) - \frac{r_0 \tan(\alpha - \theta)}{\tan \alpha} \right] \tag{4}$$

$$D_2 = D_1 - 2[l_0 \tan(\alpha - \theta)] = 2 \left[(r_0 + b) - \frac{(r_0 + b) \tan(\alpha - \theta)}{\tan \alpha} \right] \tag{5}$$

The laser energy attenuation is caused by the absorption, reflection and scattering of laser energy by the powder particles. Therefore, the number of powder particles N_p in the laser-powder interaction zone is an important parameter to determine the laser energy attenuation. The laser energy attenuation rate can be defined as the ratio of the particle projection area to the laser spot area [8], as shown in Eq. (6):

$$\mu_p = \frac{P_a}{P} = \frac{S_p}{S_L} = N_p \frac{r_p^2}{R^2} \tag{6}$$

where μ_p is the laser energy attenuation rate, P_a is the laser power attenuated by powder particles, P is the laser power, S_p and S_L are the powder particle projection and laser spot area respectively, R is the laser spot radius and N_p is the number of powder particles in the interaction between the laser beam and powder stream. Also:

$$N_p = \frac{Q_m \Delta t}{\frac{4}{3} \pi r_p^3 \rho_p} \tag{7}$$

$$\Delta t = \frac{Z - l_1}{v_p} \tag{8}$$

where Q_m is the amount of powder per unit time, Δt is the elapsed time for the powder from the upper focus to the

substrate, Z is the distance from the powder outlet to the substrate and v_p is the particle velocity.

If the volume fraction of powder particles in the powder stream exceeds a certain threshold, the powder particles below the overlapping zone cannot fully absorb the laser energy because the laser beam is vertically irradiated and the powder particles overlap with each other, so that they cannot completely melt or not melt. The laser energy attenuation calculated by the number N_p or assuming that the powder particles do not overlap each other [12, 24] is plainly inaccurate. Hence, the effective particle number \bar{N}_p is introduced to accurately calculate the laser energy attenuation rate [8], as shown in Eq. (9):

$$\bar{N}_p = M \left[1 - \left(\frac{M-1}{M} \right)^{N_p} \right] \tag{9}$$

$$M = \frac{\pi R^2}{\pi r_p^2} \tag{10}$$

where M is the projected area ratio of the laser beam and a single spherical powder particle on the forming surface.

The laser energy attenuation can then be obtained:

$$\mu_p = \bar{N}_p \frac{r_p^2}{R^2} \tag{11}$$

2.2 Modelling the cladding characteristics

The energy input and output during the LPF-AM process follows the law of energy conservation. The energy output of the

laser irradiates the powder stream, with powder particles absorb the heat, partial powder melting and deposition occurs, and the remaining laser energy is absorbed by the substrate after being affected by the powder stream reflection, thermal convection, radiation and the reflection and heat conduction of the substrate. The energy conservation in the LPF-AM process is shown in Fig. 2, and the energy relation satisfies Eq. (12):

$$E_{out} = E_P + E_{PL} + E_S + E_{SL} \tag{12}$$

where E_{out} denotes the energy output of the laser; E_P is the energy acting on the powder stream; E_{PL} denotes the energy loss caused by several factors, including the powder stream reflection, refraction and thermal convection; E_S is the energy absorbed by the substrate and E_{SL} denotes the energy consumption of due to several factors, including the substrate reflection and heat conduction.

This paper uses a Gaussian mode laser [12] with an intensity distribution described Eq. (13), and the energy consumed by the powder stream can be expressed as Eq. (14):

$$P(r) = \frac{2P}{\pi R^2} \exp\left(\frac{-2r^2}{R^2}\right) \tag{13}$$

$$E_P = \mu_P \iint_{x^2+y^2 \leq R^2} P(r)_{x,y} dx dy t - E_{PL} \tag{14}$$

where $P(r)$ is the laser energy density at position r , which is the distance to the centre point of the laser beam, and t is the processing time, which can be obtained from the following:

$$t = \frac{L}{V} \tag{15}$$

The energy loss of the laser beam as it passes through the powder stream can be expressed as:

$$E_{PL} = E_{Pre} + E_{Pc} + E_{Pra} \tag{16}$$

where E_{Pre} is the energy reflected and refracted by the powder stream, E_{Pc} is the heat convection energy loss of the powder

stream and E_{Pra} is the heat radiation energy loss of the powder stream.

The laser energy reflected and refracted by the powder stream can be expressed as:

$$E_{Pre} = \delta Q_m t E_P \tag{17}$$

The energy loss due to heat convection and radiation is:

$$E_{Pc} = h(T_{melt(P)} - T_{room}) \tag{18}$$

$$E_{Pra} = \sigma \varepsilon (T_{melt(P)}^4 - T_{room}^4) \tag{19}$$

where δ , h , σ and ε are the reflection and refraction coefficient, heat convection coefficient of the powder (usually expressed as $h = 24.1 \times 10^{-4} \varepsilon T^{1.61}$), Stefan-Boltzmann constant and radiation rate, respectively. The energy loss of the powder stream is mainly determined by the thermo-physical properties, powder particle surface area and quantity [28]. Considering previous assumptions (1) and (3), e_{PL} is defined as the lost energy per milligramme of powder. Upon combining with practical experience and experimental results, it is set as a fixed value of 0.2 J/mg [12], so that the E_{PL} can be represented as:

$$E_{PL} = Q_m t e_{PL} \tag{20}$$

In the case of single-track cladding, the energy absorbed by the powder stream should be equal to its temperature change which was from the ambient temperature T_{room} to the melting temperature T_{melt} . So it was written as [20]:

$$E_P = \rho_P A_C L [C_{(P)}(T_{melt(P)} - T_{room}) + L_{f(P)}] \tag{21}$$

where ρ_P is the powder density, A_C is the cladding area, L is the length of the cladding and $C_{(P)}$, $T_{melt(P)}$ and $L_{f(P)}$ are the specific heat, melting point and fusion latent heat of the powder, respectively.

The cladding area A_C can then be obtained:

$$A_C = \frac{\mu_P \iint_{x^2+y^2 \leq R^2} P(r)_{x,y} dx dy t - Q_m t e_{PL}}{\rho_P L [C_{(P)}(T_{(P)} - T_{room}) + L_{f(P)}]} \tag{22}$$

According to assumption (4), the effective energy E_M absorbed by the molten pool can be expressed as:

$$E_M = E_P + E_S = \eta(1 - \mu_P) P t \tag{23}$$

where η is the effective energy absorption rate of the molten pool, which only contains the energy required by the molten pool and the fusion latent heat. Also, η is determined by a variety of factors (e.g. the different material properties [29], thermal conductivity [30] and process parameters [31]), and due to the complexity of the absorption modelling, the laser wavelength, molten pool composition and processing parameter range are assumed to have a constant value of $\eta = 0.13$ [32]. Also:

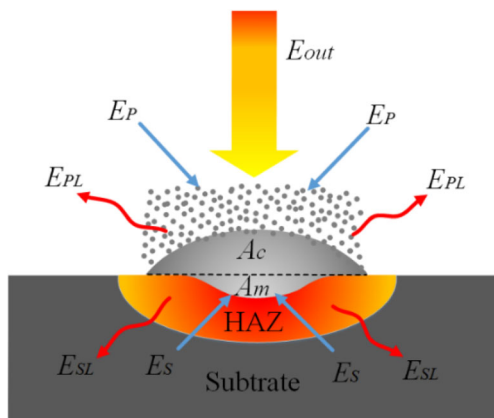


Fig. 2 Energy conservation in the LPF-AM process

$$E_M = \rho_P A_C L [C_{(P)}(T_{(P)} - T_{room}) + L_{f(P)}] + \rho_S A_m L [C_{(S)}(T_{(S)} - T_{room}) + L_{f(S)}] \tag{24}$$

where ρ_s , $C_{(s)}$, $T_{(s)}$ and $L_{f(s)}$ are the density, specific heat, melting point and fusion latent heat of the molten pool of the substrate, respectively, and A_m is the mixing area.

Therefore, the mixing area A_m can be extracted by combining Eqs. (22)~(24):

$$A_m = \frac{\eta(1-\mu_P)Pt - [\mu_P \iint_{x^2+y^2 \leq R^2} P(r)_{x,y} dx dy t - Q_m t e_{PL}]}{\mu_P \iint_{x^2+y^2 \leq R^2} P(r)_{x,y} dx dy t - Q_m t e_{PL}} \tag{25}$$

The dilution rate is defined as the ratio of the mixing area to the forming area, as shown in Eq. (26). With a decrease in the dilution rate, the mixing area decreases, which leads to a low bonding force between the cladding layer and substrate, and the cladding layer easily delaminates and falls off [23]. As the dilution rate is too large, the effect of the substrate on the composition dilution of the cladding layer increases, which causes the expected performance to decrease; moreover, cracks and other defects are prone to occur during processing. An ideal dilution rate (2%~10%) is the key to cladding layer forming and performance improvement [33].

$$D = \frac{A_m}{A_c + A_m} \tag{26}$$

3 Materials and experimental procedures

A high-strength and wear-resistant FeCr alloy powder with a particle size of 45~150 μm is deposited on AISI 4340 with a size of 40 mm × 30 mm × 20 mm by an LPF-AM experimental system. The chemical composition and thermo-physical properties of the FeCr alloy powder and AISI 4340 are shown in Tables 1 and 2, respectively. This system includes a continuous Laserline LDM-3000 photonics fibre laser with an output power range from 10~3000 W. The carrier and a shielding gas are high-purity argon with stream rates of 5 L/min and 10 L/min respectively. Upon combining the practical experience and the geometric characteristics of the powder stream, the distance between the powder outlet and the substrate is set as $Z = 40$ mm. After the LPF-AM process, the specimens are

cut, ground, polished and etched (4% nitric acid alcohol) and placed on a KEYENCE VHX-5000 optical microscope to the measure geometric characteristics. The microstructure is observed by a ZEISS Axio Scope A1 microscope with magnification from 200 to 500 times. The micro-hardness of the different zones comprising the substrate, HAZ, mixing and cladding zone is measured using Akashi’s MVK-H11 micro-hardness metre with a load of 500 gf (HV0.5) for a dwell time of 10 s. The size of the coaxial powder nozzle structure and process parameters is shown in Table 3.

4 Results and discussion

4.1 Energy and powder density

During the cladding formation in LPF-AM, the laser input energy and the forming quality are mainly influenced by the laser power, scanning velocity and powder feed rate. In this paper, single-track cladding LPF-AM experiments are carried out based on the Taguchi method, as shown in Table 4. The surface laser energy density $E = [P/(\pi R^2)] (2R/V)$ [34] and powder density $Q = Q_m/V$, which describe the laser energy per unit area and powder quality per unit length, respectively, are adopted to address the process and validate the analytical models by comparing the modelled and measured values.

The experimental results indicate that when the laser energy and powder density are insufficient, the molten pool does not have enough energy to melt all of the incoming powder. The forming quality is unsatisfactory, the cladding width is narrow and the additional unmelted powder particles are attached to the cladding layer, as shown in Fig. 3a. If the energy density is increased separately, an uneven melting width is readily formed, and the substrate surface absorbs a large amount of energy and becomes overburned, as shown in Fig. 3b. The performance of the substrate is substantially affected by an increase in the size of the mixing area and HAZ. When increasing the energy and powder density at the same time, it can be seen in Fig. 3c that multiple molten pools become stacked on each other, the molten pool size and the mobility increase, and spreading to both sides results in an increased cladding width, increased dilution rate and poorer forming quality. As Fig. 3d clearly demonstrates, if the energy density is reduced too much, there are additional unmelted powder particles that adhere to the cladding layer. Therefore,

Table 1 Chemical composition of the FeCr alloy powder and AISI 4340 (wt%)

Element	Cr	Si	B	Cu	Mo	Ni	C	P	S	Mn	Fe
FeCr alloy	16.79	4.0	3.5	3.0	3.0	2.14	0.23	0.007	0.005	—	Bal.
AISI 4340	1.5	0.25–0.30	—	—	0.2	1.55	0.34	—	—	0.5	Bal.

Table 2 The FeCr alloy powder and AISI 4340 thermo-physical properties

Thermo-physical properties	Density ρ (kg/m ³)	Melting temperature T (°C)	Latent heat of fusion L_f (J/mg)	Specific heat capacity C (J/g °C ⁻¹)
FeCr alloy	8050	1020	0.3	0.47 (20 °C)–0.79 (1020 °C)
AISI 4340	7850	1440	0.3	0.45 (20 °C)–0.70 (1440 °C)

Table 3 Structural size of the coaxial powder feeding nozzle and process parameters

Parameters	Values	Parameters	Values
Laser power (P)	1000, 1200, 1400, 1600 (W)	Powder particle velocity (v_p)	1000 mm/s
Process velocity (V)	10, 12, 14, 16 (mm/s)	Included angle (α)	20°
Powder feed rate (Q_m)	300, 400, 500, 600 (mg/s)	Divergence angle (θ)	2°
Laser spot radius (R)	2 (mm)	Powder outlet radius (r_0)	13 mm
Cladding length (L)	30 (mm)	Ambient temperature (T_0)	20 °C

the selection of the laser energy and powder density directly affects the extent of powder melting, molten pool fluidity and interlayer bonding, all of which determines the cladding forming quality. The appropriate energy and powder density are shown in Fig. 3e, which is the key to realizing net shaping during the LPF-AM process.

Adding the material properties to the analytical models in Section 2.2, the relationship between the energy and powder density and the cladding characteristics is achieved separately. Figure 4a shows that the cladding area increases as the laser energy and powder density increase. This phenomenon occurs via the large laser-powder interaction area, and as additional powder particles that melt into the molten pool, the cladding width and area increase. The substrate energy absorption increases and the mixing area increases as the laser energy density increases, but when the threshold is reached, the increase in the size of the molten pool prevents the energy from reaching the substrate, resulting in a decrease in the mixing area and dilution rate. Figure 4b shows that as the powder density increases, the mixing area and dilution

rate gradually decrease. This is caused by an increase in the size of the molten pool and the quantity of powder particles, which makes the laser energy attenuation obvious.

According to the results from the single-track cladding LPF-AM experiments, the accuracy of the analytical models with different process parameters is verified. The calculation results and experimental measurement data are shown in Fig. 5, from which it can be seen that there are differences between the model calculation results and the experimental measurement data, but the variation trends are consistent. The reasons for these differences are listed below:

- (1) The thermo-physical properties (such as the density and heat capacity) change with the temperature. In this paper, the cladding area increases with a high energy density, which may be attributed to the thermo-physical properties that are based on the mean values over the temperature range. The temperature of the laser-powder interaction area increases significantly, which is ignored, resulting in a large change

Table 4 Experimental scheme of single-track cladding laser melt deposition

Index	P (W)	V (mm/s)	Q_m (mg/s)	Index	P (W)	V (mm/s)	Q_m (mg/s)
1	1000	10	300	9	1400	10	500
2	1000	12.5	400	10	1400	12.5	600
3	1000	15	500	11	1400	15	300
4	1000	17.5	600	12	1400	17.5	400
5	1200	10	400	13	1600	10	600
6	1200	12.5	300	14	1600	12.5	500
7	1200	15	600	15	1600	15	400
8	1200	17.5	500	16	1600	17.5	300

Fig. 3 Morphology of cladding layer with different energy and powder stream densities. (a) $E = 21.22 \text{ J/mm}^2$, $Q = 33.33 \text{ mg/mm}$, (b) $E = 44.56 \text{ J/mm}^2$, $Q = 33.33 \text{ mg/mm}$, (c) $E = 50.93 \text{ J/mm}^2$, $Q = 60 \text{ mg/mm}$, (d) $E = 25.46 \text{ J/mm}^2$, $Q = 60 \text{ mg/mm}$, (e) $E = 35.65 \text{ J/mm}^2$, $Q = 48 \text{ mg/mm}$

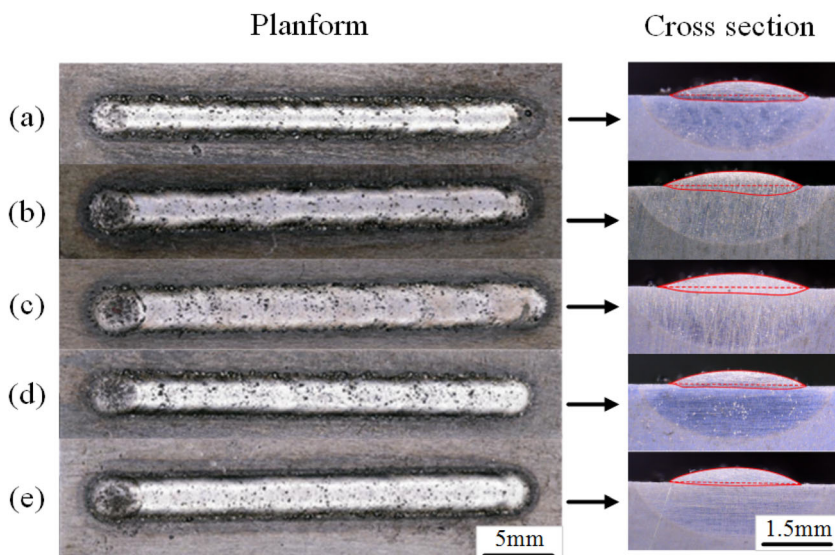
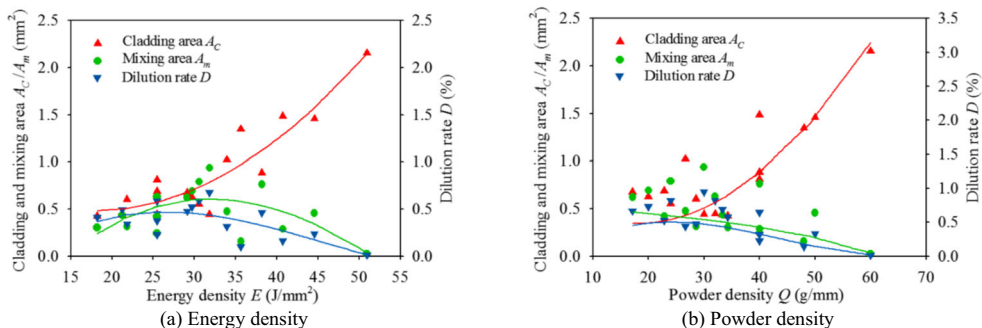


Fig. 4 Effects of energy and powder stream density on the cladding layer



in the thermo-physical properties that may highly contribute to the discrepancies.

- (2) The influence of the carrier and shielding gases on the powder stream, molten pool formation and energy dissipation is ignored.
- (3) After the measurement, the HAZ area is approximately 4~7 times that of the cladding area; therefore, it is possible that the heat conduction of the substrate may be one of the reasons for the disagreement between the

measured and predicted mixing areas and dilution rate, as shown in Fig. 5b and c.

4.2 Microstructure

To obtain ideal forming while reducing the dilution rate and ensuring the mechanical properties of the cladding layer, microstructure observations are made by selecting the best

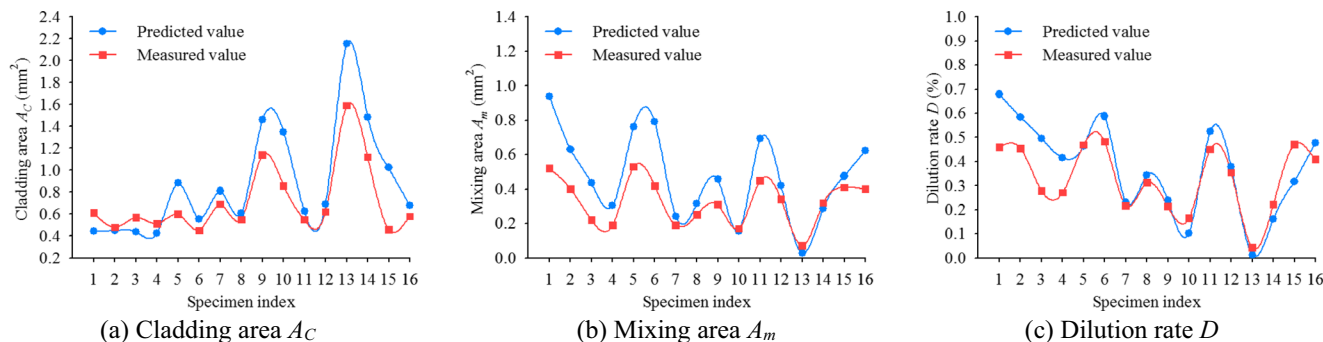


Fig. 5 Data comparison between model prediction and experiment measurement

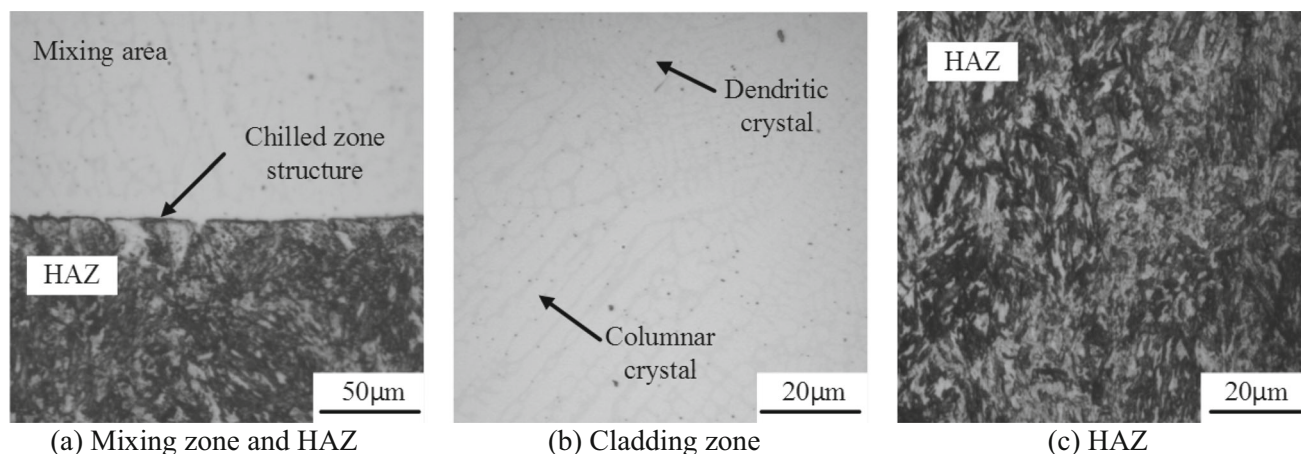


Fig. 6 Microstructure of forming area

forming specimen ($P = 1400$ W, $V = 12.5$ mm/s, $Q_m = 600$ mg/s, as shown in Fig. 3e) with a dilution rate of 7.4%. Figure 6 shows the microstructure morphology of the forming zone. As shown in Fig. 6a, the mixing zone and the HAZ form a layer comprising the chilled zone structure that shows a good metallurgical bonding. From the mixing zone to the cladding zone, the crystal morphology develops from planar crystals to cellular crystals and dendritic crystals. Liu et al. [35] suggested that the morphology transition is due to the difference in the G/R ratio (G represents the temperature gradient and R represents the solidification rate) at different locations during solidification. In the process of LPF-AM and subsequent rapid solidification, the G/R ratio in the mixing zone, HAZ, and in the vicinity of the bonding interface is extremely high, giving rise to columnar dendritic growth. As the solidification front moves towards the surface, the G/R ratio decreases and the primary arm of the columnar dendrite becomes much shorter than the dendrite in the bottom region due to the section effect and the change in the growth direction. Figure 6c shows that the HAZ is a non-layered structure composed of ferrite and cementite, which is derived from the austenitization of the crystal structure after laser irradiation and has a high strength and tenacity. In general, the microstructure of the forming

zone is dense without microcracks, and the mixing zone shows good metallurgical bonding with the substrate.

4.3 Micro-hardness

Figure 7 shows the micro-hardness profile along the upward direction of the specimen described in Section 4.3. The testing points extended from the cladding layer to the substrate. The micro-hardness value of the cladding zone is between 583 and 627 HV, and the mixing zone hardness ranges from 423 to 552 HV, which is significantly higher than the substrate hardness that ranges from 321 to 387 HV. The reason for this trend is that the alloying elements in the FeCr powder lead to an enhancement in the solid solution strengthening between the elements inside the cladding layer. Diffusion bonds form in the area between the molten pool and the HAZ, so there appears to be a transition. Laser quenching is carried out in the HAZ at elevated temperatures so that the micro-hardness there is lower than that of the mixing zone but slightly higher than that of the substrate.

5 Conclusions

- (1) To avoid the influence of powder particle overlap in the laser-powder interaction zone on the laser energy attenuation rate, multi-parameter analytical models for LPF-AM cladding geometric characteristics were established based on the laser energy attenuation rate and the law of energy and mass conservation by introducing an effective particle number. According to the experimental results of single-track cladding LPF-AM of FeCr alloy, the validity of the models for the cladding area, mixing area and dilution rate was verified.
- (2) The trends for the process parameters and geometric characteristics were analysed based on the laser energy density and powder density. Within the discussed

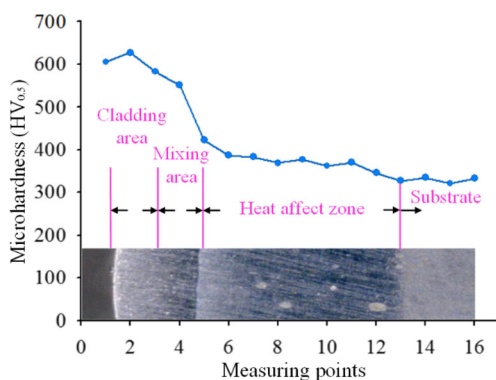


Fig. 7 The micro-hardness curve of a specimen

parameter ranges, the laser energy density and powder density had a proportional effect on the cladding area. The mixing area and dilution rate were negatively correlated with the powder density and first increased and then decreased with increasing energy density.

- (3) The microstructure and micro-hardness of the FeCr alloy LPF-AM specimen were observed under the condition of the optimal parameter combination ($P = 1400$ W, $V = 12.5$ mm/s, $Q_m = 600$ mg/s). The results showed that the mixing zone had good metallurgical bonding with the substrate, no microcracks and other defects. The micro-hardness from the mixing zone to the cladding zone ranged from 423–627 HV, which was obviously improved compared with the substrate micro-hardness.

References

- Gorunov AI (2018) Complex refurbishment of titanium turbine blades by applying heat-resistant coatings by direct metal deposition. *Eng Fail Anal* 86:115–130
- Jiang QY (2019) Improvement of microstructure, hardness, and mechanical properties of cobalt-based amorphous coating via laser cladding. *Strength Mater* 51(3):450–461
- Li YX, Su KQ, Bai PK, Liu B, Su HW, Du WB (2019) Effect of TiBCN content on microstructure and properties of laser cladding Ti/TiBCN composite coatings. *Met Mater Int* 25:166–1377
- Liu YF, Weng F, Bi GJ, Chew YX, Liu SB, Ma GY, Moon SK (2019) Characterization of wear properties of the functionally graded material deposited on cast iron by laser-aided additive manufacturing. *Int J Adv Manuf Technol* 105:4097–4105
- Wang WJ, Fu ZK, Cao X, Guo J, Liu QY, Zhu MH (2016) The role of lanthanum oxide on wear and contact fatigue damage resistance of laser cladding Fe-based alloy coating under oil lubrication condition. *Tribol Int* 94:470–478
- Zhang P, Zhang DZ, Peng DH, Li ZH, Mao ZH (2018) Rolling contact fatigue performance evaluation of Ti–6Al–4V parts processed by selective laser melting. *Int J Adv Manuf Technol* 96:3533–3543
- Hu DM, Kovacevic R (2003) Sensing, modeling and control for laser-based additive manufacturing. *Int J Mach Tools Manuf* 43: 51–60
- Wang JH, Han FZ, Chen SF, Ying WS (2019) A novel model of laser energy attenuation by powder particles for laser solid forming. *Int J Mach Tools Manuf* 145:103440
- Lalas C, Tsirbas K, Salonitis K, Chryssolouris G (2006) An analytical model of the laser clad geometry. *Int J Adv Manuf Technol* 32: 34–41
- Fathi A, Toyserkani E, Khajepour A, Durali M (2006) Prediction of melt pool depth and dilution in laser powder deposition. *J Phys D Appl Phys* 39:2613–2623
- Campanelli SL, Angelastro A, Signorile CG, Casalino G (2016) Investigation on direct laser powder deposition of 18 Ni (300) marage steel using mathematical model and experimental characterization. *Int J Adv Manuf Technol* 89:885–895
- Wang XL, Deng DW, Hu YB, Liu ZC, Zhang HC (2017) Analytical modeling and experimental investigation of laser clad geometry. *Opt Eng* 56(9):096104
- Barekat M, Shoja R, Ghasemi A (2016) Nd:YAG laser cladding of Co-Cr-Mo alloy on γ -TiAl substrate. *Opt Laser Technol* 80:145–152
- Ansari M, Shoja R, Barekat M (2016) An empirical-statistical model for coaxial laser cladding of NiCrAlY powder on Inconel 738 superalloy. *Opt Laser Technol* 86:136–144
- Nabhani M, Shoja R, Barekat M (2018) An empirical-statistical model for laser cladding of Ti-6Al-4V powder on Ti-6Al-4V substrate. *Opt Laser Technol* 100:265–271
- Mohammad E, Hassan AP, Hamidreza MS, Shoja R (2016) An empirical-statistical model for laser cladding of WC-12Co powder on AISI 321 stainless steel. *Opt Laser Technol* 97:180–186
- Ocelik V, Nenadl O, Palavra A, Hosson D (2014) On the geometry of coating layers formed by overlap. *Surf Coat Technol* 242:54–61
- Nenadl O, Kuipers W, Koelwijn N, Ocelik V (2016) A versatile model for the prediction of complex geometry in 3D direct laser deposition. *Surf Coat Technol* 307:292–300
- Huang YZ, Khamesee B, Toyserkani E (2016) A comprehensive analytical model for laser powder-fed additive manufacturing. *Addit Manuf* 12:90–99
- Shi JJ, Zhu P, Fu GY, Shi SH (2018) Geometry characteristics modeling and process optimization in coaxial laser inside wire cladding. *Opt Laser Technol* 101:341–348
- Reddy L, Preston SP, Shipway PH, Davis C, Hussain T (2018) Process parameter optimisation of laser clad iron based alloy: predictive models of deposition efficiency, porosity and dilution. *Surf Coat Technol* 349:198–207
- Liu HM, Qin XP, Huang S, Hu ZQ, Ni M (2018) Geometry modeling of single track cladding deposited by high power diode laser with rectangular beam spot. *Opt Lasers Eng* 100:38–46
- Xi WC, Song BX, Zhao Y, Yu TB, Wang J (2019) Geometry and dilution rate analysis and prediction of laser cladding. *Int J Adv Manuf Technol* 103:4695–4702
- Zhu SC, Chen WL, Ding LP, Zhan XH, Chen Q (2019) A mathematical model of laser cladding repair. *Int J Adv Manuf Technol* 103:3265–3278
- Jouvard JM, Grevey DF, Lemoine F, Vannes AB (1997) Continuous wave Nd:YAG laser cladding modeling: a physical study of track creation during low power processing. *J Laser Appl* 9:43–50
- Partes K, Seefeld T, Sepold G, Vollertsen F (2005) Increased efficiency in laser cladding by optimization of beam intensity and travel speed. *Proc SPIE* 615700:1–11
- Tabernero I, Lamikiz A, Martínez S, Ukar E, Lacalle LN (2012) Modelling of energy attenuation due to powder flow-laser beam interaction during laser cladding process. *J Mater Process Technol* 212:516–522
- Wang Q, Li JY, Gouge M, Michaleris P, Reutzal EW (2017) Physics-based multivariable modeling and feedback linearization control of melt-pool geometry and temperature in directed energy deposition. *J Manuf Sci Eng* 139:021013
- Kaplan AFH (2014) Laser absorptivity on wavy molten metal surfaces: categorization of different metals and wavelengths. *J Laser Appl* 26(1):012007
- Zhang ZD, Huang YZ, Kasinathan AR, Shahabad SL (2019) 3-dimensional heat transfer modeling for laser powder-bed fusion additive manufacturing with volumetric heat sources based on varied thermal conductivity and absorptivity. *Opt Laser Technol* 109: 297–312
- Matthews M, Trapp J, Guss G, Rubenchik A (2018) Direct measurements of laser absorptivity during metal melt pool formation associated with powder bed fusion additive manufacturing processes. *J Laser Appl* 30(3):032302
- Pinkerton AJ, Li L (2004) An analytical model of energy distribution in laser direct metal deposition. *Proc Inst Mech Eng B J Eng Manuf* 218(4):363–374

33. Yan SX, Dong SY, Xu BS, Wang ZJ, Zhang XD, Liu WH (2011) Characterization and optimization of process in laser cladding Fe314 alloy. *Infrared Laser Eng (in Chinese)* 40(2):235–240
34. Wu CL, Zhang S, Zhang CH, Zhang H, Dong SY Phase evolution and properties in laser surface alloying of FeCoCrAlCuNi_x high-entropy alloy on copper substrate. *Surf Coat Technol* 315:368–376
35. Liu H, Hao JB, Han ZT, Yu G, He XL, Yang HF (2016) Microstructural evolution and bonding characteristic in multi-layer laser cladding of NiCoCr alloy on compacted graphite cast iron. *J Mater Process Technol* 232:153–164

Publisher's note Springer Nature remains neutral with regard to jurisdictional claims in published maps and institutional affiliations.